CRYSTAL GROWTH & DESIGN

pubs.acs.org/crystal

Article

Shape-Controlled Synthesis of Cu_3TeO_6 Nanoparticles with Photocatalytic Features

Javier Fernández-Catalá,* Laura Jussila, Matyas Daboczi, Filipp Temerov, Salvador Eslava, Rossella Greco, and Wei Cao

Cite This: https://doi.org/10.1021/acs.cgd.3c00929

Read Online

ACCESS | Metrics & More | Article Recommendations | Supporting Information

ABSTRACT: Cu_3TeO_6 (CTO) has been synthesized by hydrothermal synthesis applying different pH values without any template or a calcination step to control the crystalline phase and the morphology of nanoparticles. The physicochemical properties characterized by X-ray diffraction, field emission scanning electron microscopy, transmission electron microscopy, N_2 adsorption, X-ray photoelectron spectroscopy, and diffuse reflectance ultraviolet−visible (DRUV−vis) spectroscopy techniques revealed that the pH values significantly influence the crystal growth. In acidic media (pH = 2), crystal growth has not been achieved. At pH = 4, the yield is low (10%), and the CTO presents irregular morphology. At pH = 6, the yield increases (up to 71%) obtaining an agglomeration of nanoparticles into spherical morphology. At basic conditions (pH = 8), the yield increases up to 90% and the morphology is the same as the sample obtained at pH = 6. At high basic conditions (pH = 10), the yield is similar (92%), although the morphology changes totally to dispersed nanoparticles. Importantly, the as-prepared CTO semiconductor presents photocatalytic activity for H_2 production using triethanolamine as a sacrificial agent under visible light illumination. The results also revealed that the nanoparticles agglomerated in a spherical morphology with larger surface area presented almost double activities in H_2 production compared to heterogeneously sized particles. These results highlight the suitable optoelectronic properties, including optical band gap, energy levels, and photoconductivity of CTO semiconductors for their use in photocatalytic H_2 production.

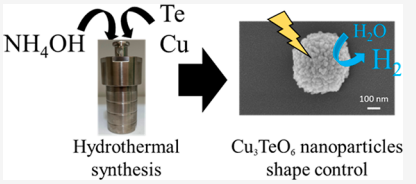

INTRODUCTION

The design and crystal growth of semiconductor materials have been drawing attention of the scientific community due to the materials' applications in photocatalysis, photosensors, and solar cells, among others.[1−3] A promising family of semiconductor materials is metal tellurates M_3TeO_6 (MTOs), which are composed of 3d transition metals (M) such as copper (Cu), nickel (Ni), cobalt (Co), tellurium (Te), and oxygen (O).[4,5] Until now magnetoelectric applications have been the main focus for the use of MTOs, due to their multiferroic properties.[6,7] Although, in the last years the scientific community has started to explore the application of these materials in the fields of photocatalysis,[5] electrochemistry,[8] and sensors,[9] among others.[10]

One fascinating compound within the MTO family is Cu_3TeO_6 (CTO).[4,11] The CTO crystal structure was first determined by Hostachy and Coing-boyat[12] and was revised in 1978.[13] This material has a cubic structure (Ia3), which is built up by TeO_6 units connected through copper atoms.[13] However, one of the main challenges of the application of MTOs for sensors, solar cells, or photocatalysis, is the synthetic procedure.[7,14] A main synthetic route relies on the solid-state synthesis, but it fails to control the Te coordination, the morphology, and the particle size of the materials.[13,15] Besides, this methodology requires high temperatures. The above pros and cons demand the shape-controllable synthesis of MTOs, such as wet chemical routes, to open the door to this family of materials to several applications.[9,16] Therefore, the emphasis has been shifted toward developing CTO materials using wet chemical methodologies, such as the coprecipitation method. In this sense, Mutharani et al. showed a facile wet chemical method to prepare CTOs for their application in an electrochemical sensor.[9] In some cases, these routes use different additives to achieve the desired composition.[4,17] However, the use of additives such as NaOH to start the precipitation and to control the morphology of the final materials can generate different phases in the target product, e.g., $Na_2Cu_2TeO_6$.[18,19] In a recent study, our research group[4] proposed the use of hydrothermal methodology to perform the synthesis of MTOs, Ni_3TeO_6 and Cu_3TeO_6, using NaOH as an additive. We obtained single-phase crystals using the hydrothermal method at pH = 7. On the other hand, the coprecipitation method at pH = 7 in the presence of NaOH leads to a multiphase in the final product. With this in mind, the design of novel synthetic strategies of MTOs, using novel

Received: August 4, 2023
Revised: October 24, 2023
Accepted: October 24, 2023

procedures such as hydrothermal synthesis to control the morphology and the MTO properties, is crucial to unveil the plethora of potential applications of MTOs.

One potential application of MTOs might be their use as photocatalysts.[20,21] Photocatalysis technology has received tremendous attention due to its promising application in renewable energy production such as H_2 generation after the pioneer work of Fujishima and Honda about water photolysis on TiO_2 electrodes in 1972.[22] Recently, the scaling up of solar H_2 production via photocatalytic overall water splitting was possible using an aluminum-doped strontium titanate particulate photocatalyst.[23] Nevertheless, the authors claimed that it is necessary to develop photocatalysts active under visible light with adequate redox potential to boost their catalytic activity. Therefore, the scientific community is developing new materials[24,25] or tuning widely known photocatalytic active semiconductors (TiO_2, ZnO, etc.)[26,27] for their application in this area. In this sense, the MTOs present great potential to be used as photocatalysts as demonstrated by their photocatalytic activity in pollutant degradation[5] or H_2 production.[10,28] Additionally, these materials can absorb visible light,[11] which represents a key point for their application in photocatalysis.

In this work, CTO nanoparticles have been synthesized by hydrothermal synthesis at different pH values using HCl and NH_4OH to control the crystal growth and develop a shape-controlled CTO without any template or a calcination step. The as-synthesized materials have been characterized by X-ray diffraction (XRD), scanning electron microscopy (SEM), transmission electron microscopy (TEM), N_2 adsorption, diffuse reflectance ultraviolet−visible (DRUV−vis) spectroscopy, and X-ray photoelectron spectroscopy (XPS), showing a change in morphology and yield of the final CTOs at different pH values, hydrothermal conditions such as temperature and time, and an eventual calcination step. The obtained CTOs have absorption in the visible range (E_g = 2.6 eV) and photocatalytic activity in H_2 production, providing a preliminary proof of concept for the use of this novel material in energetic applications.

EXPERIMENTAL SECTION

Materials. Copper nitrate ($Cu(NO_3)_2 \times 3H_2O$, 99−104%, Sigma-Aldrich), telluric acid (H_6O_6Te, 98%, Sigma-Aldrich), ammonia solution (NH_4OH, 25%, Sigma-Aldrich), absolute ethanol (EtOH, 99.5%, ETAX), and deionized (DI) water were used in the present work. All reactants were used as received without any further purification.

Materials Preparation. CTOs were prepared by hydrothermal synthesis using $Cu(NO_3)_2 \times 3H_2O$ and H_6O_6Te as reagents with different synthetic conditions, such as pH, hydrothermal conditions, and for comparison, a calcination step. In a typical procedure, $Cu(NO_3)_2 \times 3H_2O$ and H_6O_6Te were mixed in a stoichiometric ratio of 3:1, respectively, in DI water (60 mL). This solution was stirred vigorously for 10 min. Then, HCl (5% v/v) or NH_4OH (5% v/v) solution was used to adjust the pH to 2, 4, 6, 8, and 10 while stirring, to study the effect of pH in the synthetic media. The solution was adjusted to the adequate pH and was stirred for a further 5 min. Afterward, this solution was transferred to a Teflon-lined stainless-steel autoclave (100 mL) and heated to 180 °C for 12 h. After that, the mixtures were centrifuged (5000 rpm) to collect the solid materials, which were washed three times with DI water and three times with EtOH to clean the samples from impurities. The obtained solids were dried under vacuum overnight. The obtained Cu_3TeO_6 powders were named CTO_X, where the "X" corresponds to the pH used during the synthesis of the MTOs. The sample prepared in acidic conditions (pH = 2) was heated to 180 °C in an autoclave for 7 days. In this acidic condition, no solid semiconductor was obtained.

To study the effect of calcination, sample CTO_8 was calcined at 600 °C for 2 h with a heating rate of 10 °C/min. The calcined sample was named CTO_Calc. To study the effect of hydrothermal temperature and time, one sample was prepared using a hydrothermal temperature of 120 °C for 6 h, and another was prepared at room temperature and ambient pressure for 12 h. The Cu_3TeO_6 powders obtained were named CTO_120_6 and CTO_RT, respectively.

Materials Characterization. The global yield values were calculated according to

$$\text{yield} = \frac{m}{m_0}$$

where m is the final mass obtained using the hydrothermal reaction and m_0 is the calculated theoretical mass. Field emission SEM (FE-SEM) images were taken using a Zeiss Ultra plus field emission scanning electron microscope. The samples were coated with Pt to avoid a charging effect in the image acquisition. TEM images coupled with energy dispersive spectroscopy (EDS) mapping were obtained using JEOL JEM-2200FS field emission transmission electron microscope/scanning transmission electron microscope. Powder XRD patterns at room temperature were obtained with a Rigaku SmartLab 9 kW equipped with a five-axis $\theta-\theta$ goniometer, 1D solid-state detector, and scintillator using Co−Kα (λ = 1.79 Å, 40 kV, 135 mA) radiation. The mean crystal size was estimated by applying the Scherrer equation[29] using the full width at half-maximum (fwhm) data of the major diffraction peak and a K factor of 0.93

$$B = \frac{K\lambda}{\beta \cos\theta}$$

where B is the crystalline size (nm); K is the dimensionless shape factor whose value is 0.93; λ is the wavelength of the radiation source used, which is 1.79 Å for Co−Kα radiation; β is the fwhm intensity (radians), and θ is the Bragg angle at the position of the peak maximum.

The specific surface areas, average pore sizes, and volumes of the synthesized materials were measured with N_2 adsorption at −195 °C using a Micromeritics ASAP 2020 surface analyzer. Before the analyses, the samples were evacuated for 4 h at 250 °C. DRUV−vis spectra were obtained using a Shimadzu UV-2600 spectrophotometer using $BaSO_4$ as a background. The surface-sensitive technique XPS was performed with Al−Kα using a Thermo Fisher Scientific ESCALAB 250Xi XPS system. Energy calibration of the XPS was performed using C 1s peak at 284.8 eV as a reference.

The valence band edge (E_v) values of the solid samples on an indium tin oxide-coated glass substrate were measured by ambient photoemission spectroscopy (APS02, KP Technology). The samples were illuminated by monochromatic UV light in the energy range of 7−4 eV and the cube root photoemission signals were extrapolated to zero to determine E_v. The optical band gap values of the samples were added to the E_v to calculate the conduction band edge (E_c) values. The Fermi level of the samples was recorded by a vibrating tip Kelvin probe (SKP5050, KP Technology). A freshly cleaned silver reference was used to determine the tip's work function.

Photoelectrochemical measurements were performed in a three-electrode setup (Ivium Compacstat potentiostat) with a Ag/AgCl reference electrode and Pt counter electrode in a 0.1 M KNO_3 aqueous electrolyte. The photoelectrodes were illuminated by a xenon lamp (Lot Quantum Design) with an AM1.5 filter and 100 mW cm^{-2} intensity through a circular mask (0.28 cm^2). The photoelectrode was prepared by drop-casting a CTO dispersion [20 mg in 0.5 mL of ethanol and 20 μL of Nafion solution (5 wt %)] on fluorine-doped tin oxide-coated glass, which was consecutively dried at 80 °C.

Photocatalytic Test. The photocatalytic H_2 production of CTO synthesized at different pH values was measured under visible light irradiation on a Perfect Light PCX50B photoreactor, following the studies reported previously by our research group.[30,31] The white LED (λ > 420 nm), employed as the irradiation source in the

https://doi.org/10.1021/acs.cgd.3c00929
Cryst. Growth Des. XXXX, XXX, XXX−XXX

photoreactor used, has a light intensity of 80 mW·cm^{-2}. The photocatalytic tests were performed in a quartz bottle with a height of 90 mm, a diameter of 35 mm, and a total volume of 68 mL. CTO semiconductors (5 mg) were suspended in a solution of DI water (25 mL) and triethanolamine (5%) as the electron donor. Before illumination with visible light, the dispersion was purged with Ar for 30 min under stirring conditions in the dark. The prepared solution was exposed to visible light for 4 h at room temperature using the Perfect Light PCX50B photoreactor. The H_2 generated was measured by an Agilent 8860 gas chromatograph equipped with a split/splitless inlet, a TCD detector, and a capillary column CP-Molsieve 5 Å 25 m × 0.53 mm × 50 mm. Additionally, a blank test without catalyst was performed under the same experimental conditions as in the catalytic tests, and no catalytic activity was detected in the absence of the photocatalyst.

RESULTS AND DISCUSSION

Materials Characterization. The yields of the samples obtained at different pH values by hydrothermal synthesis without a template using HCl and NH_4OH were calculated and are depicted in Scheme 1. Successful synthesis in acid

Scheme 1. Scheme of Hydrothermal Procedure to Synthesize CTO at Different pH Values, Indicating the Morphologies and the Yields Obtained

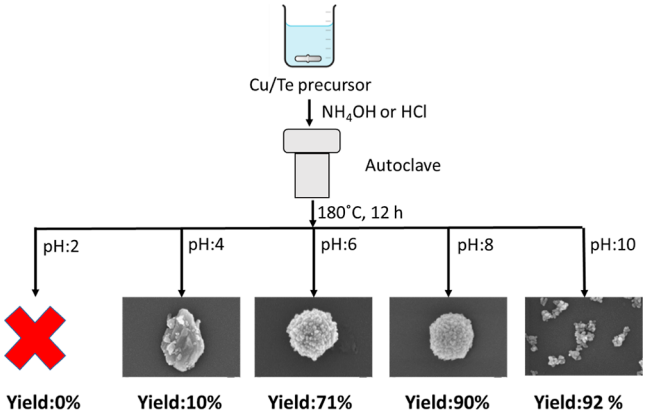

media (pH = 2) is not observed or leads to a very low yield of 10% at pH = 4. However, at pH = 6, the obtained yield presents a great increase up to 71% and this trend is followed in basic conditions, which bring to yields of around 90 and 92% for pH = 8 and pH = 10, respectively. The results indicate that the pH value has a great effect on the synthesis of CTOs. This effect might be related to the fact that in acidic conditions copper was dissolved in an aqueous environment as Cu^{2+} ions, and with the increase of the pH, copper started to precipitate in the form of $Cu(OH)_2$ as suggested by the Pourbaix diagram described by Celante and Freitas.[32] The results suggest that for the synthesis of CTO, it is recommendable to use neutral or basic pH conditions to start the precipitation of copper with the further possibility to obtain Cu_3TeO_6. The growth of this crystal is enabled by the coordination of $Cu(OH)_2$ with Te. On the other hand, in acidic media, copper cannot be stabilized in a crystal structure and is kept dissolved as Cu^{2+} as suggested by the Pourbaix diagram; thus, the crystal growth is not possible. Herein, we demonstrated the relevance of the pH value for the synthesis of semiconductors using wet chemistry methodologies as observed in previous reports.[32−34]

The crystal structures of the CTOs synthesized at different pH values were studied by XRD analysis (Figure 1).

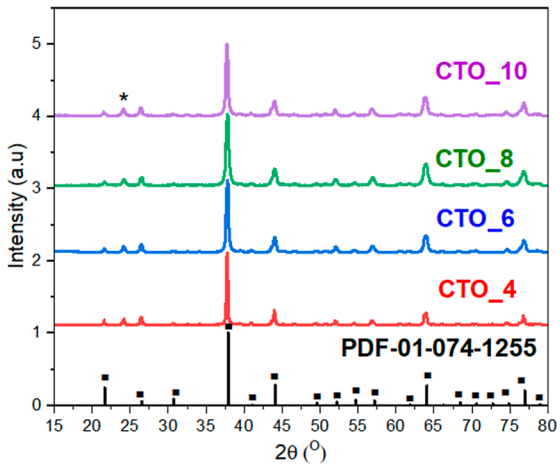

Figure 1. XRD patterns of CTOs synthesized by using different pH values. Square-ended bars indicate the position and relative intensity of Cu_3TeO_6 reflections (PDF-01-074-1255). (*) indicates the position of $Cu_3TeO_6{\cdot}H_2O$ reflection (PDF-00-047-1751).

Independently from the pH synthesis media, all the samples prepared in this work showed the characteristic diffraction peaks at 2θ = 20.93, 25.90, 30.10, 37,25, 43.42, 54.07, 56.52, 63.48, 70.05, and 76.377°, corresponding to the characteristic peaks of (200), (211), (220), (222), (400), (422), (431), (440), (600), and (622) lattice planes of Cu_3TeO_6 (PDF 01-074-1255), respectively, and related to Cu_3TeO_6 crystalline single phase.[35] However, the samples also show a characteristic diffraction peak at 2θ = 24.24° corresponding to the characteristic peak of (210) of mineral mcalpineite "$Cu_3TeO_6 \times H_2O$". This fact indicates that the CTO synthesized by hydrothermal methodology presents both phases due to the aqueous environment which allows for the incorporation of water molecules in the crystal structure of Cu_3TeO_6 as previously reported in the literature.[36] Moreover, the crystallite sizes of the MTOs synthesized at different pH values were calculated using the Scherrer equation. The results indicate that upon acidic conditions (pH = 4) a bigger crystallite grain size (76.2 nm) was formed while the CTO synthesized at higher (basic) pH such as pH = 6, pH = 8, and pH = 10 had crystallite grain sizes of 30.1 26.4, and 29.7 nm, respectively. These calculations indicate that the pH of the reaction media has a great influence on the crystalline size as it will be further displayed with microscopic analysis results.

The morphology of the samples prepared by hydrothermal synthesis using different pH values (CTO_4, CTO_6, CTO_8, and CTO_10) have been studied by SEM and TEM. The SEM micrographs (Figure 2) show that the pH of hydrothermal synthesis had a great effect on the morphology of the materials as previously reported for several other semiconductors.[37−39] The sample synthesized at acidic pH (pH = 4) had an irregular size (160 nm). The morphology in Figures 2a and S1a demonstrates heterogeneous size and shape, with an average size of 160 nm (Figure S1a). However, at pH = 6 or 8, the observed materials revealed a homogeneously dispersed size and spherical morphology due to the agglomeration of smaller nanoparticles in these specific synthetic conditions as shown in Figure 2b,c. The sample CTO_6 is formed by nanoparticles with a smaller size (24 nm) (Figure S1b) and aggregated to form spherical particles with an average size of 388 nm (Figure S2a). The same effect was observed for the CTO_8 sample, which exhibited a slight

https://doi.org/10.1021/acs.cgd.3c00929
Cryst. Growth Des. XXXX, XXX, XXX−XXX

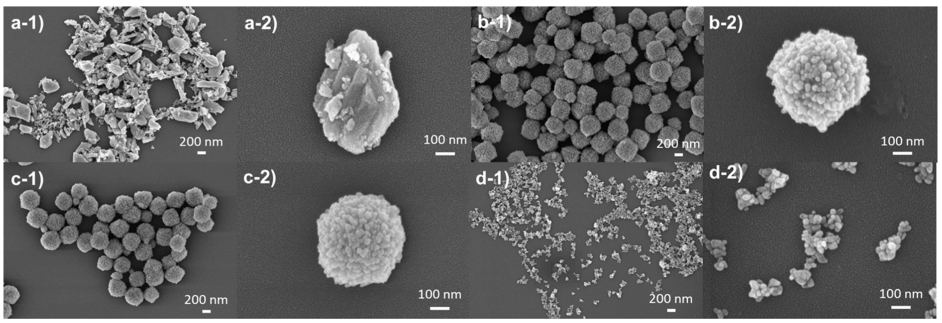

Figure 2. SEM micrographs of CTOs prepared at different pH values: (a) 4, (b) 6, (c) 8, and (d) 10.

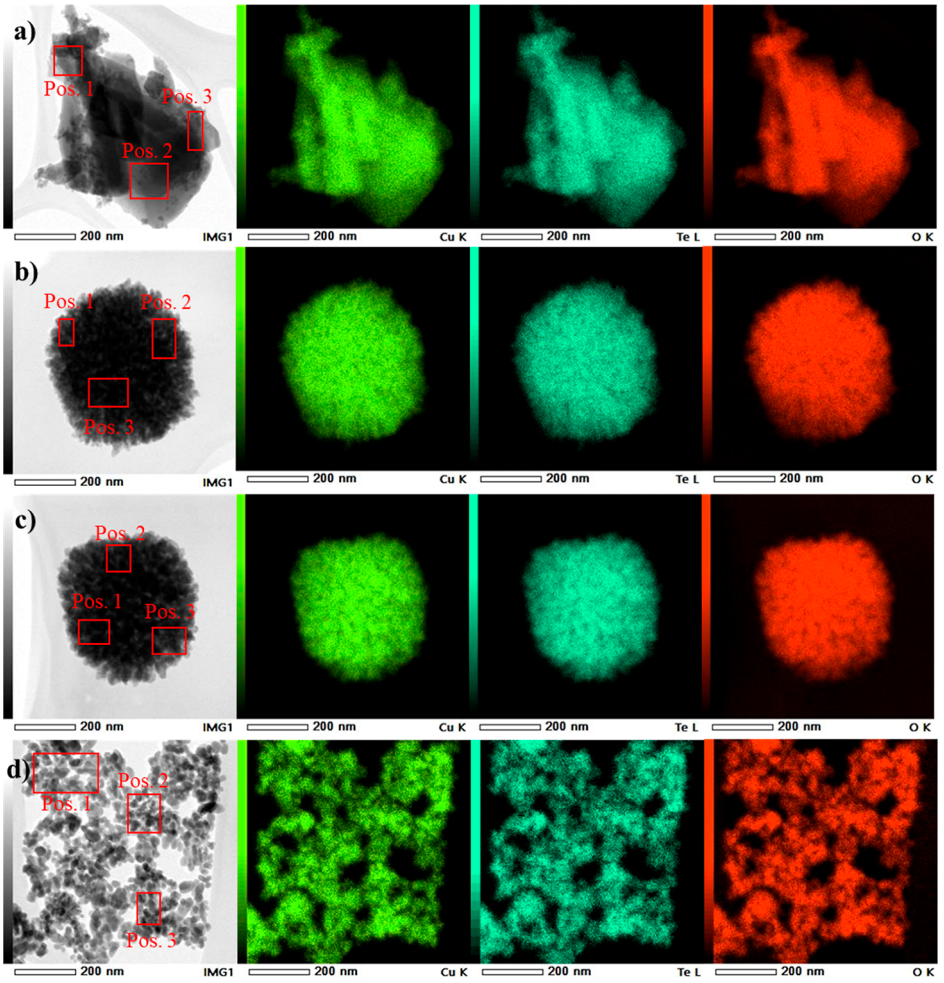

Figure 3. STEM images and corresponding EDS mapping images of Cu (green), Te (blue), and O (red) elements. (a) STEM image and elemental mapping images of CTO_4. (b) STEM image and elemental mapping images of CTO_6. (c) STEM image and elemental mapping images of CTO_8. (d) STEM image and elemental mapping images of CTO_10.

increase in the size of the nanoparticles (26 nm) (Figure S1c) and in the size of the spherical agglomerations (390 nm) (Figure S2b) with respect to the CTO_6 sample. At basic synthetic conditions (pH = 10), the sample CTO_10 presents a homogeneously dispersed nanoparticle size (28 nm) (Figure S1d) without aggregation in spherical morphology (see Figure 2d). To confirm the result obtained by SEM, the samples were also analyzed by TEM (Figure S3). TEM analysis was consistent with the results obtained by SEM since sample CTO_4 presents an irregular morphology. Furthermore, the samples CTO_6 and CTO_8 have a spherical morphology due to the agglomeration of small nanoparticles as was observed by SEM analysis. Also, it is observed that sample CTO_10 possesses a nanoparticle morphology without agglomeration in spherical particles, contrary to CTO_6 and CTO_8. The SEM and TEM results indicated that the pH condition in the hydrothermal synthesis of MTOs substantially affects the morphology, size, and crystallinity of the tellurates. Moreover, SEM and TEM images show that at pH = 6 and pH = 8 the nanoparticles tend to aggregate to decrease the surface energy. Indeed, it is well-known and has been already reported that the surface energy is minimal on spheric-shaped morphologies.[38,40]

The elemental composition of the CTO samples (Figure 1g) was analyzed by STEM-EDS. The STEM images (Figure 3)

https://doi.org/10.1021/acs.cgd.3c00929
Cryst. Growth Des. XXXX, XXX, XXX−XXX

show the same morphology dependent on the pH media used as was observed by SEM and TEM analyses. The EDS mappings (Figure 3) of the samples show only the presence of Cu (green), Te (blue), and O (red) elements homogeneously distributed in the sample, regardless of the morphology obtained. The relative amount obtained by EDS of the elements Cu and Te is lower (Table S1) with respect to O compared with the stoichiometric ratio (Cu_3TeO_6) and our previously reported results.[4] This fact might indicate the presence of both phases (Cu_3TeO_6 and $Cu_3TeO_6{\cdot}H_2O$) in the samples synthesized in this work as it was observed by XRD analysis, since the $Cu_3TeO_6{\cdot}H_2O$ material has a higher stoichiometrical amount of O in its elemental structure.

The porous texture of the synthesized samples was investigated by N_2 adsorption measurements (Figure 4).

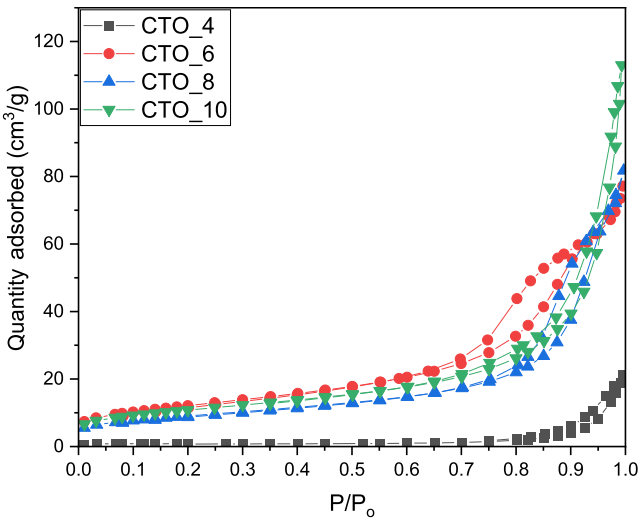

Figure 4. N_2 isotherms at 77 K for the samples prepared in this study at different pH values.

CTO_4 sample synthesized at acidic conditions revealed a type II isotherm, typical of nonporous materials.[41] The CTO_6 sample had a type IV isotherm, indicating that the structure is mesoporous due to the agglomeration of nanoparticles in spherical morphology as observed by SEM and TEM analyses. Moreover, the CTO_8 sample showed a type IV isotherm indicating that the material is mesoporous.[42,43] However, the hysteresis of the CTO_8 samples was significantly smaller than sample CTO_6 implying a change in the mesoporosity of this sample.[42] The CTO_10 sample had a type IV isotherm although the hysteresis decreased. Indeed, at these synthetic conditions, the sample presents a nanoparticle morphology without aggregation of nanoparticles in spheres as it was previously described by SEM.[43] Concerning the textural properties shown in Table 1, the changes in the synthetic conditions, focusing on the pH, have a great impact on the surface area of the materials. The CTO_4 sample synthesized in acidic media had a low surface area indicating that this material is nonporous with big particle sizes as was observed by N_2 adsorption isotherms and SEM analysis. The samples synthesized at higher pH (6, 8, and 10) demonstrated an increase in the surface area. The CTO_6 sample showed a higher surface area (43.1 m^2/g) due to the small nanoparticles observed by SEM and the space generated between the particles in the spherical agglomerations.[44] However, the increase in the pH value, in the samples CTO_8 and CTO_10, corresponds to a decrease in the surface area to 36.1 and 36 m^2/g, respectively, probably due to the loss of the spherical features and to the change in the mesoporosity as indicated by the change in the hysteresis of the isotherms (Figure 4).

Table 1. Textural Properties of CTOs Prepared at Different pH Values

samples	S_{BET} (m^2/g)	$V_{total,0.95}$ (cm^3/g)	V_{N2DR} (cm^3/g)
CTO_4	2.2	0.025	0.0014
CTO_6	43	0.115	0.0316
CTO_8	36	0.112	0.029
CTO_10	36	0.167	0.0257

The chemical composition and the oxidation states of the elements in the prepared samples and the optical absorption properties were analyzed by XPS and DRUV−vis analysis, respectively. The XPS analysis of Cu 2p level (Figure 5a) for the samples prepared at different pH shows a peak at 933.7 eV and a satellite peak at 940.1 eV for CTO_4, CTO_6, CTO_8, and CTO_10, indicating the presence of Cu^{2+}.[11] Also, in all the samples prepared using hydrothermal synthesis a peak at 936.66 eV is observed, indicating the presence of $Cu(OH)_2$[45] on the surface of the material due to the use of wet chemistry conditions, more specifically of aqueous environment. The presence of $Cu(OH)_2$ in the CTO samples prepared by hydrothermal synthesis was observed and described previously in our recent work.[4] In this work, the analysis of Te 3d XPS spectra for the CTO samples was performed (Figure S4a), despite the fact that the analysis is challenging due to the Cu-auger peak appearing at the same range (569.2 eV). To solve this problem, the Cu-auger peak was fitted to obtain the correct background and to successfully perform the analysis of Te 3d XPS peaks. Te 3d XPS spectra showed two peaks at 575.8 and 576.9 eV, indicating the presence of Te^{4+} and Te^{6+}, respectively. The mix valence between Te^{4+} and Te^{6+} was recently reported by Numan et al. for Ni_3TeO_6[46,47] and observed in our recent report.[4] The O 1s XPS spectra of CTO samples showed a main peak at 530.46 eV assigned to the oxygen present in Cu_3TeO_6 lattices. Additionally, a shoulder at 531.3 eV indicates the possible presence of −OH on the surface of CTO samples or oxygen vacancies in agreement with Cu 2p XPS analysis and with the previous results reported by our group[4] and the group of Numan et al.[46,47] Finally, the results of XPS for the CTO materials synthesized at different pH values revealed the presence of Cu^{2+}, Te^{4+} and Te^{6+}, which might be generated by the possible oxygen vacancies.[46,47] Moreover, the presence of −OH functional groups on the surface of the samples, even at pH = 4, indicates that the $Cu(OH)_2$ intermediate might be crucial for the synthesis of CTOs as was observed following the yield of the synthesis.

The DRUV−vis spectra of the samples prepared at different pH values are shown in Figure 5b. All CTO samples showed two absorption ranges and an abrupt cutoff in the range of 200−500 nm as common in semiconductors.[4,11] The band gaps (E_g) determined by Tauc plot analysis[48] (Figure S5) demonstrate that the sample synthesized at acidic pH (CTO_4) had a lower band gap (2.46 eV) than the samples prepared at higher pH (CTO_6:2.6 eV, CTO_8:2.59 eV, and CTO_10:2.53 eV). The DRUV−vis results indicated that CTO is a semiconductor with a band gap in the range of the visible (2.6 eV), which is a very intriguing property for its use as a photocatalyst in visible light-mediated processes.[5,20,49]

https://doi.org/10.1021/acs.cgd.3c00929
Cryst. Growth Des. XXXX, XXX, XXX−XXX

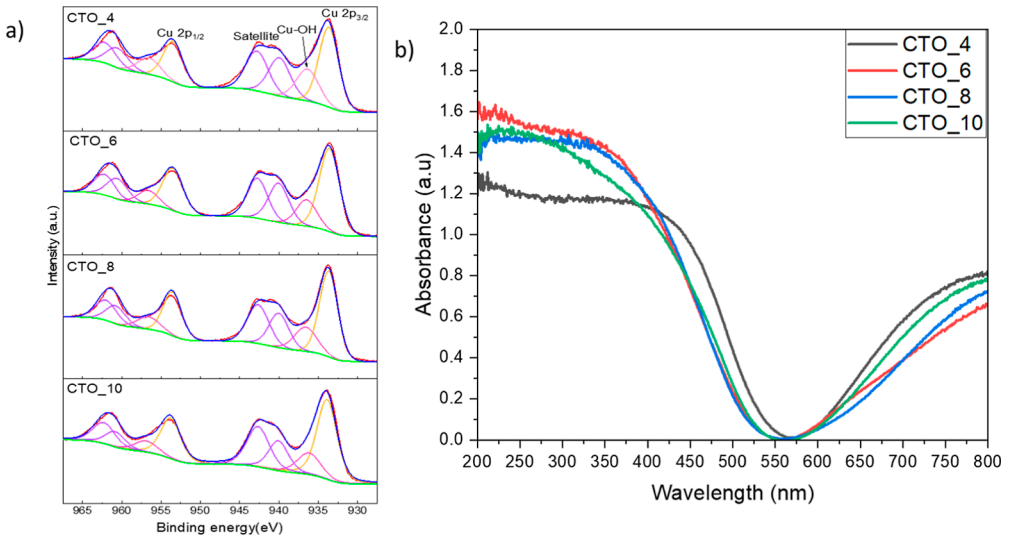

Figure 5. (a) XPS spectra of Cu 2p and (b) DRUV−vis spectra of samples prepared in this work at different pH values.

Based on the above results, a possible scheme of the formation mechanism of the Cu_3TeO_6 materials prepared in this work using hydrothermal synthesis might be expressed as follows

$$Cu^{2+} + 2OH^- \rightarrow Cu(OH)_2 \quad (1)$$

$$3Cu(OH)_2 + H_6O_6Te \rightarrow Cu_3TeO_6 + 6H_2O \quad (2)$$

To start the growth of the crystals, the copper ions present in the solution are likely to be coordinated with the ion hydroxide to form copper hydroxide ($Cu(OH)_2$). Then, copper hydroxide reacts with tellurium precursor (H_6O_6Te). The temperature and the pressure achieved in the hydrothermal conditions lead to the formation of crystals of copper tellurate (Cu_3TeO_6), following the mechanism previously reported for several inorganic materials using hydrothermal synthesis.[50,51] This mechanism is proposed since in acidic media (pH = 2) the synthesis of MTOs is not achieved even after performing the reaction for 1 week. At pH = 4, the material is synthesized but the yield of the reaction is very low (10%) and also in this case the functional group −OH and extra phase $Cu_3TeO_6{\cdot}H_2O$ were observed by XPS and XRD analysis, respectively. When a base (NH_4OH) was used in the solution, the yield of the reaction increased to 71% (CTO_6), 90% (CTO_8), and 92% (CTO_10). This fact indicates the great effect of OH^- ions in the synthesis of MTOs. Another proof supporting this possible mechanism is that the Pourbaix diagram described by Celante and Freitas[32] indicates that at pH higher than ∼6 the Cu^{2+} starts the coordination and later precipitates in the form of $Cu(OH)_2$ in agreement with our observations. This points toward the importance of $Cu(OH)_2$ as a possible intermediate in the formation of CTO.

In this work, the effects of hydrothermal methodology (temperature and time) and the calcination effect on CTO materials were studied. To study the effect of the calcination step, sample CTO_8 was calcined at 600 °C (CTO_Calc). Furthermore, the effect of hydrothermal conditions such as temperature and time was studied, using a hydrothermal temperature of 120 °C for 6 h (CTO_120_6) or room temperature and ambient pressure for 12 h (CTO_RT) to study the effect of the hydrothermal synthesis (see the Experimental Section). The powder XRD analysis of the samples prepared with different conditions demonstrated different crystalline properties as shown in Figure 6. The

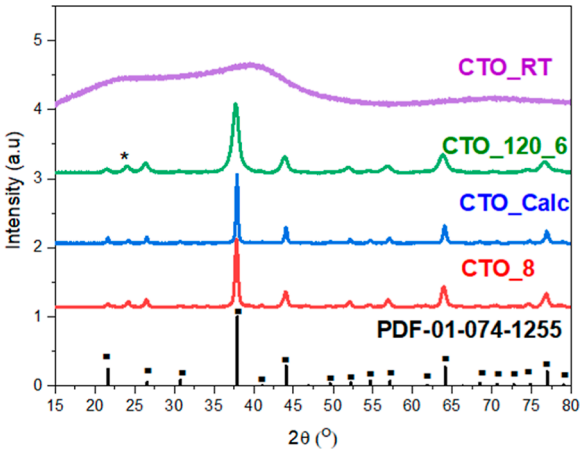

Figure 6. XRD patterns of CTO materials using different synthetic conditions (hydrothermal and calcination temperature). Square-ended bars indicate the position and relative intensity of Cu_3TeO_6 reflections (PDF-01-074-1255). (*) indicates the position of $Cu_3TeO_6{\cdot}H_2O$ reflection (PDF-00-047-1751).

sample calcined at 600 °C had the same crystalline phases as the sample without calcination (CTO_8). However, the intensity of the diffraction peak at 2θ = 24.24°, which corresponds to the characteristic peak of (210) of mineral mcalpineite "$Cu_3TeO_6{\cdot}H_2O$", decreases with respect to sample CTO_8. This fact could be explained by the possible removal of H_2O from the crystalline structure or by the elimination of the −OH functional groups present on the surface of the CTO_8 sample during the calcination step. Additionally, after the calcination step the crystalline grain of the sample increased from 26.4 (CTO_8) to 40.1 nm (CTO_8_Calc). The treatment with high temperature led to an enlargement of the particles as previously observed in several semiconductors, such as TiO_2.[44,52] Regarding the effect of the hydrothermal treatment, it is observed that the sample CTO_120_6 presents the same crystalline phase as CTO_8, indicating that the crystalline phase of Cu_3TeO_6 can be obtained at a lower

https://doi.org/10.1021/acs.cgd.3c00929
Cryst. Growth Des. XXXX, XXX, XXX−XXX

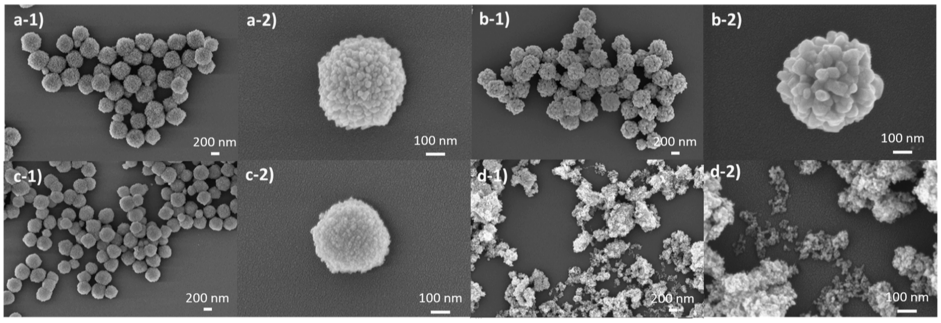

Figure 7. SEM micrographs of CTOs prepared at different conditions (hydrothermal and calcination step): (a) CTO_8, (b) CTO_8_Calc, (c) CTO_120_6, and (d) CTO_RT.

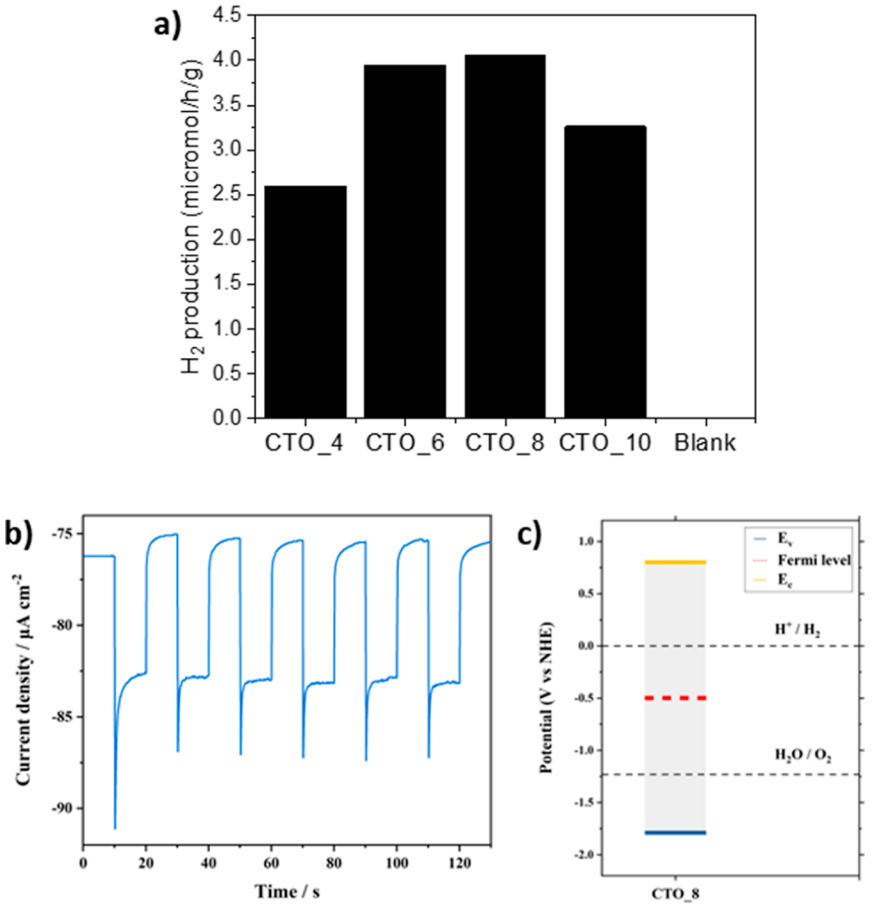

Figure 8. (a) H_2 production of CTO samples prepared at different pH values and blank test without a catalyst (blank). (b) Photocurrent generated by a CTO_8 photoelectrode under chopped 1 sun illumination in an aqueous 0.1 M KNO_3 electrolyte at 0 V vs the reversible hydrogen electrode. (c) Comparison of the measured energy levels of CTO_8 to the electrochemical potential of water oxidation and reduction.

hydrothermal temperature in only 6 h without the calcination step. However, the crystalline size of this sample is 10.8 nm, which indicates that the increase in temperature and time leads to an increase in the size and in the crystallinity of the MTOs as previously reported for other inorganic materials.[53] The XRD analysis of sample CTO_RT prepared at room temperature and pressure shows that this sample is amorphous. This fact highlights the importance of hydrothermal synthesis to obtain crystalline CTOs.

The morphology of the CTO_8_Calc, CTO_ 120_6, and CTO_RT samples has been studied by SEM (Figure 7) and compared with that of CTO_8 (Figure 7a). The SEM images of the sample CTO_8_Calc (Figure 7b) show that the calcination step increases the nanoparticles size from 26 (Figure S1c) to 64 nm (Figure S6a) as was observed by XRD, maintaining the spherical size due to the agglomeration of the particles. The CTO_120_6 sample (Figures 7c and S6b) has a smaller size (11 nm) than CTO_8 (26 nm), confirming the great effect of hydrothermal conditions detected also by XRD analysis. The sample prepared at room pressure and temperature (CTO_RT) shows a heterogeneous morphology, indicating that the use of the hydrothermal methodology is inevitable for shape control of the morphology. Indeed, the high temperature and pressure obtained in the autoclave when using this methodology[51,54] allow the formation of crystals with well-defined shapes and morphology. The calcination

https://doi.org/10.1021/acs.cgd.3c00929
Cryst. Growth Des. XXXX, XXX, XXX−XXX

effect on the porous texture of the Cu_3TeO_6 samples was determined by N_2 adsorption measurements (Figure S7 and Table S2). As shown in Figure S7, the sample calcined at 600 °C shows a sintering effect and, as a consequence, a loss of porosity, validating the XRD and SEM results. Regarding the textural properties of the calcined sample, this sample presents a low surface area due to the sintering effect of the nanoparticles as observed in the literature for TiO_2.[44] The structural analysis of CTO using different synthetic parameters as the calcination step, different times and temperatures in hydrothermal synthesis, and synthesis at room temperature and pressure indicates that these parameters dramatically affect the synthesis of MTOs. In this sense, the results show that a calcination step was not necessary to obtain the crystalline MTOs. However, considering that at room temperature and pressure the materials obtained were amorphous, the use of hydrothermal synthesis is mandatory to reach crystalline MTOs due to the high pressures and temperatures generated in the autoclaves. Moreover, in this study, the significance of the hydrothermal parameters was underlined. An increase in the time and in the temperature of the hydrothermal treatment enhances crystallinity and size of the nanoparticles; hence, the hydrothermal conditions affect the final structural properties of CTO material.

The effect of the copper precursor ($CuNO_3$, $CuCl_2$, and $CuSO_4$) in the hydrothermal synthesis of CTO semiconductors was also studied. The results obtained by XRD and SEM show that the copper precursor does not change the crystalline phase (Figure S8) and the morphology (Figure S9) of the synthesized CTO. This fact indicates that the Cu precursor does not have a relevant effect on the hydrothermal synthesis of the MTOs.

Photocatalytic H_2 Production Activity of CTO Samples. The CTO semiconductors synthesized at different pH values absorb visible light, have large surface areas, and have high surface groups on the surface. Thus, CTO semiconductors are employed in photocatalytic water splitting. The catalytic tests showed that the CTOs synthesized in this work are capable of producing H_2 using triethanolamine (5% v/v) as an electron donor under visible light irradiation (see Figure 8a). Furthermore, the results (Figure 8a) show that the pH in the hydrothermal synthesis affects the photocatalytic activity: CTO_6 and CTO_8 show better catalytic activity than CTO_4 and CTO_10. This fact might be related to the spherical morphology obtained for the samples synthesized at pH = 6 and pH = 8. Consequently, the morphology based on nanoparticles agglomerated in spheres (CTO_6 and CTO_8) provides a mesoporous catalyst and a small particle size of CTOs to boost the H_2 production as previously reported for other photocatalysts.[55] These results highlight the importance of the surface area in photocatalysis since the nonporous CTO_4 sample with 2.2 m^2/g of BET area does not present high amount of produced H_2. On the other hand, CTO_6 (43 m^2/g of BET area) and CTO_8 (36 m^2/g of BET area) samples showed improved photocatalytic results. These results also underline another relevant feature of the materials presented in this work, i.e., the porosity. To an increase of the mesoporosity corresponds an easier diffusion of the reagents, and consequently, an enhanced catalytic activity as it was described previously in the literature.[56] Therefore, this would explain the boosted catalytic activity in CTO_6 and CTO_8 (spherical morphology) samples with respect to CTO_10 (nanoparticle morphology) and CTO_4 (irregular morphology). In other words, the presence of mesoporosity in CTO_6 and CTO_8 generated by the space between the particles in the spherical agglomerations, as was observed by N_2 adsorption and SEM analysis, results in a higher H_2 production. Furthermore, in the photocatalytic tests, it is noticeable that the sample synthesized at pH = 10 presents higher activity than the sample synthesized at pH = 4. This is in line with morphologic determinations in SEM (Figure 2) and textural properties obtained by N_2 adsorption analysis (Table 1) where the larger surface areas provide more reaction sites for photocatalysis. The photocatalytic activity of CTO was further confirmed by observing significant (~17 $\mu A/cm^2$) photocurrent generation by CTO photoelectrodes in an aqueous electrolyte at 0 V vs the reversible hydrogen electrode (see Figure 8b). Finally, the energy band diagram of CTO_8 was built based on APS and Kelvin probe measurements (see Figure 8c). The E_v value of CTO_8 at −1.79 V vs the normal hydrogen electrode is below the water oxidation potential, while the E_c at 0.8 V vs the normal hydrogen electrode is above the hydrogen evolution reaction potential with a Fermi level in the middle of the band gap. Such energy levels are desirable for photocatalysts used for solar water splitting and confirm the suitability of the CTO for photocatalytic H_2 production. Overall, these results provide a preliminary proof of concept for the use of CTO for future energetic applications, such as photocatalytic H_2 production.

CONCLUSIONS

In conclusion, shape-controlled hydrothermal synthesis of Cu_3TeO_6 using NH_4OH as the alternative base to NaOH was demonstrated without a calcination step. The hydrothermal synthesis conditions have a great effect on the final properties of the CTOs. In this sense, the use of basic pH to synthesize CTO materials with high crystallinity and high yield is evidenced as shown by experiments carried out at different pH values in the hydrothermal synthesis of CTO. Importantly, XRD and XPS results unveiled that $Cu(OH)_2$ is a possible intermediate in the hydrothermal synthesis of CTOs.

The morphology and size of the CTO nanoparticles were observed and analyzed by SEM and XRD and could be tuned not only by modifying the synthetic conditions such as pH but also by changing the hydrothermal conditions (temperature and time) or adding a calcination step. However, to obtain crystalline MTOs at low temperatures, a hydrothermal synthesis procedure is necessary considering that an amorphous material was obtained when the synthesis was performed at room temperature and pressure.

The CTOs fabricated in this work using hydrothermal synthesis demonstrated photocatalytic activity in H_2 production in the presence of triethanolamine as an electron donor. The photocatalytic tests showed that the morphology of the synthesized nanostructures affects the catalytic activity. Samples synthesized at pH = 6 and pH = 8 showed spherical morphology and the highest photocatalytic activity. This work opens up the possibility of synthesizing MTOs with different morphologies to be applied in energetic applications, such as photocatalysis and photoelectrochemical devices.

ASSOCIATED CONTENT

Supporting Information

The Supporting Information is available free of charge at https://pubs.acs.org/doi/10.1021/acs.cgd.3c00929.

https://doi.org/10.1021/acs.cgd.3c00929
Cryst. Growth Des. XXXX, XXX, XXX−XXX

Size distribution histogram of CTO samples, TEM images, EDS spectroscopy analysis, XPS spectra of Te 3d and O 1s, Tauc plot of CTO samples, N_2 isotherms at 77 K and textural properties, and XRD patterns and SEM images of CTO samples prepared with different precursors (PDF)

AUTHOR INFORMATION

Corresponding Author

Javier Fernández-Catalá − *Nano and Molecular Systems Research Unit, University of Oulu, Oulu FIN-90014, Finland; Materials Institute and Inorganic Chemistry Department, University of Alicante, Alicante E-03080, Spain;* orcid.org/0000-0002-8570-2655; Email: j.fernandezcatala@ua.es

Authors

Laura Jussila − *Nano and Molecular Systems Research Unit, University of Oulu, Oulu FIN-90014, Finland*

Matyas Daboczi − *Department of Chemical Engineering and Centre for Processable Electronics, Imperial College London, London SW7 2AZ, U.K.;* orcid.org/0000-0001-9920-3657

Filipp Temerov − *Nano and Molecular Systems Research Unit, University of Oulu, Oulu FIN-90014, Finland*

Salvador Eslava − *Department of Chemical Engineering and Centre for Processable Electronics, Imperial College London, London SW7 2AZ, U.K.;* orcid.org/0000-0002-2416-3205

Rossella Greco − *Nano and Molecular Systems Research Unit, University of Oulu, Oulu FIN-90014, Finland;* orcid.org/0000-0001-6408-1645

Wei Cao − *Nano and Molecular Systems Research Unit, University of Oulu, Oulu FIN-90014, Finland;* orcid.org/0000-0003-3139-1780

Complete contact information is available at: https://pubs.acs.org/10.1021/acs.cgd.3c00929

Author Contributions

Javier Fernández-Catalá: investigation, conceptualization, methodology, and writing—original draft. **Laura Jussila:** acquisition and analysis of XPS data. **Matyas Daboczi:** acquisition and analysis of APS and photocurrent results, and writing—review and editing. **Filipp Temerov:** acquisition of APS and writing—review and editing. **Salvador Eslava:** writing—review and editing. **Rossella Greco:** catalytic test analysis, conceptualization, methodology, and writing—review and editing. **Wei Cao:** supervision, funding acquisition, and writing—review and editing.

Notes

The authors declare no competing financial interest.

ACKNOWLEDGMENTS

JFC thanks MARSALAS21-09 grant funded by MCIN/AEI/10.13039/501100011033 and European Union NextGeneration EU/PRTR. S.E. and M.D. thank the EPSRC grant EP/S030727/1 for financial support. Financial support from the ERC (European Research Council) Consolidator Grant CATCH (grant agreement no 101002219) is also acknowledged. The authors thank Dr. Romain Botella for his help in the data management and relevant discussion about the project. Authors gratefully acknowledge the Centre for Material Analysis (CMA), University of Oulu for characterizations and Dr. Harishandra Singh for discussion and initialization of MTO materials research at NANOMO unit.

REFERENCES

(1) Roy, P.; Berger, S.; Schmuki, P. TiO_2 nanotubes: Synthesis and applications. *Angew. Chem., Int. Ed.* **2011**, *50*, 2904−2939.

(2) Tong, H.; Ouyang, S.; Bi, Y.; Umezawa, N.; Oshikiri, M.; Ye, J. Nano-photocatalytic materials: Possibilities and challenges,. *Adv. Mater.* **2012**, *24*, 229−251.

(3) Patil, A. S.; Patil, A. V.; Dighavkar, C. G.; Adole, V. A.; Tupe, U. J. Synthesis techniques and applications of rare earth metal oxides semiconductors: A review. *Chem. Phys. Lett.* **2022**, *796*, 139555.

(4) Fernández-Catalá, J.; Singh, H.; Wang, S.; Huhtinen, H.; Paturi, P.; Bai, Y.; Cao, W. Hydrothermal synthesis of Ni_3TeO_6 and Cu_3TeO_6 nanostructures for magnetic and photoconductivity applications. *ACS Appl. Nano Mater.* **2023**, *6*, 4887−4897.

(5) Xu, L.; Qin, C.; Xie, H.; Huang, Y.; Qin, L.; Seo, H. J. Ilmenite-type semiconductor Ni_3TeO_6: Preparation, optical property and photo-degradation ability. *Mater. Lett.* **2016**, *184*, 1−4.

(6) Oh, Y. S.; Artyukhin, S.; Yang, J. J.; Zapf, V.; Kim, J. W.; Vanderbilt, D.; Cheong, S.-W. Non-hysteretic colossal magneto-electricity in a collinear antiferromagnet. *Nat. Commun.* **2014**, *5*, 3201.

(7) Mathieu, R.; Ivanov, S. A.; Nordblad, P.; Weil, M. Enhancement of antiferromagnetic interaction and transition temperature in M_3TeO_6 systems (M = Mn, Co, Ni, Cu). *Eur. Phys. J. B* **2013**, *86*, 361.

(8) Park, S.; Park, S.; Mathew, V.; Sambandam, B.; Hwang, J. Y.; Kim, J. A new tellurium-based Ni_3TeO_6-carbon nanotubes composite anode for Na-ion battery. *Int. J. Energy Res.* **2022**, *46*, 16041−16049.

(9) Mutharani, B.; Rajakumaran, R.; Chen, S. M.; Ranganathan, P.; Chen, T. W.; Al Farraj, D. A.; Ajmal Ali, M.; Al-Hemaid, F. M. A. Facile synthesis of 3D stone-like copper tellurate (Cu_3TeO_6) as a new platform for anti-inflammatory drug ibuprofen sensor in human blood serum and urine samples. *Microchem. J.* **2020**, *159*, 105378.

(10) Iqbal, M. Z.; Carleschi, E.; Doyle, B. P.; Kriek, R. J. Dark current water splitting employing Ni_3TeO_6 as a photocharged photo-electrocatalyst. *Phys. Status Solidi* **2023**, *220*, 2300002.

(11) Mardolkar, S. D.; Salker, A. V. Insulator-semiconductor transitions and photo-luminescent behaviour in doped copper tellurates. *Mater. Sci. Semicond. Process.* **2020**, *105*, 104758.

(12) Hostachy, A.; Coing-boyat, J. Structure crystalline de Cu_3TeO_6. *C. R. Acad. Sci.* **1968**, *267*, 1435.

(13) Falck, B. Y. L.; Lindqvist, O.; Bataillon, P. E. Tricopper(II) Tellurate(VI). *Acta Crystallogr.* **1978**, *18*, 896−897.

(14) Singh, H.; Sinha, A. K.; Gupta, S. M.; Singh, M. N.; Ghosh, H. Insight into the growth reaction mechanism of ceramic Co_3TeO_6: Synchrotron structural and thermal analysis. *J. Am. Ceram. Soc.* **2016**, *99*, 3443−3448.

(15) Sankar, R.; Shu, G. J.; Karunakara Moorthy, B.; Jayavel, R.; Chou, F. C. Growing of fixed orientation plane of single crystal using the flux growth technique and ferrimagnetic ordering in Ni_3TeO_6 of stacked 2D honeycomb rings. *Dalton Trans.* **2013**, *42*, 10439−10443.

(16) Chen, J.; Ma, Q.; Wu, X. J.; Li, L.; Liu, J.; Zhang, H. Wet-Chemical Synthesis and Applications of Semiconductor Nanomaterial-Based Epitaxial Heterostructures. *Nano-Micro Lett.* **2019**, *11*, 86.

(17) Hussain, R. A.; Hussain, I. Metal telluride nanotubes: Synthesis, and applications,. *Mater. Chem. Phys.* **2020**, *256*, 123691.

(18) Murtaza, T.; Kalaivanan, R.; Madeswaran, G.; Bayikadi, K.; Sankar, R. Magnetic properties of honeycomb spin lattice compounds $Na_2M_2TeO_6$ (M = Co, Ni) and spin dimer compound $Na_2Cu_2TeO_6$ single crystals by flux-growth. *J. Mater. Res. Technol.* **2021**, *14*, 1601−1608.

(19) Xu, J.; Assoud, A.; Soheilnia, N.; Derakhshan, S.; Cuthbert, H. L.; Greedan, J. E.; Whangbo, M. H.; Kleinke, H. Synthesis, structure, and magnetic properties of the layered copper (II) oxide $Na_2Cu_2TeO_6$. *Inorg. Chem.* **2005**, *44* (14), 5042−5046.

https://doi.org/10.1021/acs.cgd.3c00929
Cryst. Growth Des. XXXX, XXX, XXX−XXX

(20) Yang, X.; Wang, D. Photocatalysis: From Fundamental Principles to Materials and Applications. *ACS Appl. Energy Mater.* **2018**, *1*, 6657−6693.
(21) Wang, Z.; Li, C.; Domen, K. Recent developments in heterogeneous photocatalysts for solar-driven overall water splitting. *Chem. Soc. Rev.* **2019**, *48*, 2109−2125.
(22) Fujishima, A.; Honda, K. Electrochemical Photolysis of Water at a Semiconductor Electrode. *Nature* **1972**, *238*, 37−38.
(23) Nishiyama, H.; Yamada, T.; Nakabayashi, M.; Maehara, Y.; Yamaguchi, M.; Kuromiya, Y.; Nagatsuma, Y.; Tokudome, H.; Akiyama, S.; Watanabe, T.; et al. Photocatalytic solar hydrogen production from water on a 100-m^2 scale. *Nature* **2021**, *598*, 304−307.
(24) Akhundi, A.; Zaker Moshfegh, A.; Habibi-Yangjeh, A.; Sillanpää, M. Simultaneous Dual-Functional Photocatalysis by g-C_3N_4-Based Nanostructures. *ACS EST Engg.* **2022**, *2*, 564−585.
(25) Habibi-Yangjeh, A.; Pournemati, K. A review on emerging homojunction photocatalysts with impressive performances for wastewater detoxification. *Crit. Rev. Environ. Sci. Technol.* **2023**, *1*, 1−31.
(26) Feizpoor, S.; Rahim Pouran, S.; Habibi-Yangjeh, A. Recent progress on photocatalytic evolution of hydrogen gas over TiO_{2-x}-based emerging nanostructures. *Mater. Sci. Semicond. Process.* **2023**, *162*, 107444.
(27) Schneider, J.; Matsuoka, M.; Takeuchi, M.; Zhang, J.; Horiuchi, Y.; Anpo, M.; Bahnemann, D. W. Understanding TiO_2 Photocatalysis: Mechanisms and Materials. *Chem. Rev.* **2014**, *114*, 9919−9986.
(28) Fernández-Catalá, J.; Kistanov, A. A.; Bai, Y.; Singh, H.; Cao, W. Theoretical prediction and shape-controlled synthesis of two-dimensional semiconductive Ni_3TeO_6. *npj 2D Mater. Appl.* **2023**, *7*, 48.
(29) Zhang, H.; Banfield, J. F. Understanding polymorphic phase transformation behavior during growth of nanocrystalline aggregates: Insights from TiO_2. *J. Phys. Chem. B* **2000**, *104*, 3481−3487.
(30) Talebi, P.; Singh, H.; Rani, E.; Huttula, M.; Cao, W. Surface plasmon-driven photocatalytic activity of Ni@NiO/$NiCO_3$ core-shell nanostructures. *RSC Adv.* **2021**, *11*, 2733−2743.
(31) Talebi, P.; Kistanov, A. A.; Rani, E.; Singh, H.; Pankratov, V.; Pankratova, V.; King, G.; Huttula, M.; Cao, W. Unveiling the role of carbonate in nickel-based plasmonic core@shell hybrid nanostructure for photocatalytic water splitting. *Appl. Energy* **2022**, *322*, 119461.
(32) Celante, V. G.; Freitas, M. B. J. G. Electrodeposition of copper from spent Li-ion batteries by electrochemical quartz crystal microbalance and impedance spectroscopy techniques. *J. Appl. Electrochem.* **2010**, *40*, 233−239.
(33) Phillips, V. A.; Kolbe, J. L.; Opperhauser, H. Effect of pH on the growth of $Mg(OH)_2$ crystals in an aqueous environment at 60°C. *J. Cryst. Growth* **1977**, *41*, 228−234.
(34) Wu, Z.; Zhou, W.; Jin, W.; Xu, N. Effect of pH on synthesis and properties of perovskite oxide via a citrate process. *AIChE J.* **2006**, *52*, 769−776.
(35) He, Z.; Itoh, M. Magnetic behaviors of Cu_3TeO_6 with multiple spin lattices. *J. Magn. Magn. Mater.* **2014**, *354*, 146−150.
(36) Missen, O. P.; Mills, S. J.; Canossa, S.; Hadermann, J.; Nenert, G.; Weil, M.; Libowitzky, E.; Housley, R. M.; Artner, W.; Kampf, A. R.; Rumsey, M. S.; Spratt, J.; Momma, K.; Dunstan, M. A. Polytypism in mcalpineite: A study of natural and synthetic Cu_3TeO_6. *Acta Crystallogr., Sect. B: Struct. Sci., Cryst. Eng. Mater.* **2022**, *78*, 20−32.
(37) Wang, Y.; Guan, X.; Li, L.; Li, G. PH-driven hydrothermal synthesis and formation mechanism of all $BiPO_4$ polymorphs. *CrystEngComm* **2012**, *14*, 7907−7914.
(38) Zhang, A.; Zhang, J.; Cui, N.; Tie, X.; An, Y.; Li, L. Effects of pH on hydrothermal synthesis and characterization of visible-light-driven $BiVO_4$ photocatalyst. *J. Mol. Catal. A: Chem.* **2009**, *304*, 28−32.
(39) Meng, X.; Zhang, L.; Dai, H.; Zhao, Z.; Zhang, R.; Liu, Y. Surfactant-assisted hydrothermal fabrication and visible-light-driven photocatalytic degradation of methylene blue over multiple morphological $BiVO_4$ single-crystallites. *Mater. Chem. Phys.* **2011**, *125*, 59−65.
(40) Yang, C.; Yang, X.; Li, F.; Li, T.; Cao, W. Controlled synthesis of hierarchical flower-like Sb_2WO_6 microspheres: Photocatalytic and superhydrophobic property. *J. Ind. Eng. Chem.* **2016**, *39*, 93−100.
(41) Thommes, M.; Kaneko, K.; Neimark, A. V.; Olivier, J. P.; Rodriguez-Reinoso, F.; Rouquerol, J.; Sing, K. S. W. Physisorption of gases, with special reference to the evaluation of surface area and pore size distribution (IUPAC Technical Report). *Pure Appl. Chem.* **2015**, *87*, 1051−1069.
(42) Sotomayor, F.; Quantatec, A. P.; Sotomayor, F. J.; Cychosz, K. A.; Thommes, M. Characterization of Micro/Mesoporous materials by physisorption: Concepts and case studies. *Acc. Mater. Surf. Res.* **2018**, *3*, 34−50. https://www.researchgate.net/publication/331260891
(43) Mendioroz, S.; Pajares, J. A.; Benito, I.; Pesquera, C.; Gonzalez, F.; Blanco, C. Texture evolution of montmorillonite under progressive acid treatment: Change from H3 to H2 type of hysteresis. *Langmuir* **1987**, *3*, 676−681.
(44) Fernández-Catalá, J.; Cano-Casanova, L.; Lillo-Ródenas, M.; Berenguer-Murcia, Á.; Cazorla-Amorós, D. Synthesis of TiO_2 with hierarchical porosity for the photooxidation of propene. *Molecules* **2017**, *22*, 2243.
(45) Vasquez, R. P. $Cu(OH)_2$ by XPS. *Surf. Sci. Spectra* **1998**, *5*, 267−272.
(46) Numan, M.; Salman Khan, M.; Majumdar, S. Vacancy induced mixed valence state in nickel tellurate Ni_3TeO_6. *Mater. Today: Proc.* **2022**, *57*, 151−156.
(47) Numan, M.; Das, G.; Khan, M. S.; Manna, G.; Banerjee, A.; Giri, S.; Aquilanti, G.; Majumdar, S. Evidence of exchange striction and charge disproportionation in the magnetoelectric material Ni_3TeO_6. *Phys. Rev. B* **2022**, *106*, 214437.
(48) Makuła, P.; Pacia, M.; Macyk, W. How To Correctly Determine the Band Gap Energy of Modified Semiconductor Photocatalysts Based on UV-Vis Spectra,. *J. Phys. Chem. Lett.* **2018**, *9*, 6814−6817.
(49) Takanabe, K. Photocatalytic water splitting: Quantitative approaches toward photocatalyst by design. *ACS Catal.* **2017**, *7*, 8006−8022.
(50) Wang, Y.; Cai, F.; Guo, P.; Lei, Y.; Xi, Q.; Wang, F. Short-Time Hydrothermal Synthesis of $CuBi_2O_4$ Nanocolumn Arrays for Efficient visible-light photocatalysis. *Nanomaterials* **2019**, *9*, 1257.
(51) Ortiz-Landeros, J.; Gómez-Yáñez, C.; López-Juárez, R.; Dávalos-Velasco, I.; Pfeiffer, H. Synthesis of advanced ceramics by hydrothermal crystallization and modified related methods. *J. Adv. Ceram.* **2012**, *1*, 204−220.
(52) Shah, A. H.; Rather, M. A. Effect of calcination temperature on the crystallite size, particle size and zeta potential of TiO_2 nanoparticles synthesized via polyol-mediated method. *Mater. Today: Proc.* **2021**, *44*, 482−488.
(53) Zhang, M.; Falvey, J.; Hector, A. L.; Garcia-Araez, N. Effects of the reaction temperature and Ba/Ti precursor ratio on the crystallite size of $BaTiO_3$ in hydrothermal synthesis. *RSC Adv.* **2022**, *12*, 27809−27819.
(54) Li, W. N.; Yuan, J.; Shen, X. F.; Gomez-Mower, S.; Xu, L. P.; Sithambaram, S.; Aindow, M.; Suib, S. L. Hydrothermal synthesis of structure- And shape-controlled manganese oxide octahedral molecular sieve nanomaterials. *Adv. Funct. Mater.* **2006**, *16*, 1247−1253.
(55) Lakshminarasimhan, N.; Bae, E.; Choi, W. Enhanced photocatalytic production of H_2 on mesoporous TiO_2 prepared by template-free method: Role of interparticle charge transfer. *J. Phys. Chem. C* **2007**, *111*, 15244−15250.
(56) Fernández-Catalá, J.; Cazorla-Amorós, D.; Berenguer-Murcia, Á. Facile encapsulation of P25 (TiO_2) in spherical silica with hierarchical porosity with enhanced photocatalytic properties for gas-phase propene oxidation. *Appl. Catal., A* **2018**, *564*, 123−132.

https://doi.org/10.1021/acs.cgd.3c00929
Cryst. Growth Des. XXXX, XXX, XXX−XXX